Journal of Materials Chemistry A

COMMUNICATION

View Article Online
View Journal | View Issue

Cite this: J. Mater. Chem. A, 2015, 3, 18847

Received 2nd July 2015
Accepted 12th August 2015

DOI: 10.1039/c5ta04936a

www.rsc.org/MaterialsA

Large-scale aligned crystalline $CH_3NH_3PbI_3$ perovskite array films†

Yitan Li,[ab] Xiao Wang,[a] Shiting Wu,[c] Haina Ci,[ab] Henglu Xu,[a] Xuemei Li,[d] Hao Sun,[e] Zeyao Zhang,[a] Anyuan Cao,[c] Xuefeng Guo[ab] and Yan Li*[ab]

Owing to the lattice match, aligned $CH_3NH_3PbI_3$ perovskite array films composed of $CH_3NH_3PbI_3$ microribbons with the length at the sub-millimeter scale were fabricated on ST cut quartz which showed a fast photo-response. This method provides a simple and flexible approach to grow oriented crystalline $CH_3NH_3PbI_3$ arrays at the millimeter scale.

Organic–inorganic hybrid lead halide perovskite ($CH_3NH_3PbX_3$, X = Cl, Br, I) based solar cells pioneered by Kojima *et al.* have obtained a significant improvement in power conversion efficiency from 3.8% to 20.1% in the past five years.[1–22] It is well known that the diffusion length of perovskite layers, which is closely related to the film crystallinity and morphology, plays a key role in the performances of the device. Numerous efforts have been made to enhance the photovoltaic performance by improving the crystallinity of $CH_3NH_3PbX_3$ films and therefore increasing the diffusion length.[2,13–17,20,23] Horváth *et al.* first prepared lead iodide perovskite ($CH_3NH_3PbI_3$) nanowires with a length up to 10 μm.[24] Shi *et al.* obtained crack-free $MAPbX_3$ single crystals exceeding 100 mm^3 in volume and observed low trap-state density and large carrier diffusion lengths above 10 μm.[23] Nie *et al.* reported solution-processed perovskite solar cells with millimeter-scale grains and recorded efficiencies approaching 18% with little cell-to-cell variability.[20]

Besides the crystallinity, it is known that the organization or the arrangements of the materials is also an important issue. For example, oriented arrays of one-dimensional single crystalline ZnO and TiO_2, compared to random polycrystalline nanostructures showed longer electron diffusion length and faster charge transport, which provides a solution to further improve the performances of solar devices.[25,26] Yet, until now, there is no report on the preparation of well-aligned lead halide perovskite crystals.

Epitaxy has shown to be a powerful strategy to prepare ordered crystalline nanostructures of a wide variety of materials such as giant magnetoresistance nanostructures, semiconducting thin films, and graphene.[27–31] Lattice match between the substrate and the target material is essential in epitaxial growth. With a suitable substrate, we may be able to epitaxially grow ordered $CH_3NH_3PbX_3$ crystals.

We find that the surface of ST cut quartz, which has been widely used to guide the growth of horizontally aligned single-walled carbon nanotube (SWNT) arrays,[32–35] shows similar structural characteristics to tetragonal $CH_3NH_3PbI_3$ as shown in Scheme 1. Along the [1 0 0] direction on the surface of ST cut quartz, which is just the direction SWNT oriented, there is a structural period with a scale of 19.65 Å (l_a). The lattice spacing of (0 0 1) planes of $CH_3NH_3PbI_3$ is 12.68 Å (d_{001}).[1] It can be found that $2l_a \approx 3d_{001}$ with a mismatch of 3.2%. (1 0 1) plane in $CH_3NH_3PbI_3$, whose dihedral angle with the (0 0 1) plane is 55.0°, present a lattice spacing of 7.30 Å (d_{101}). In the surface lattice of ST cut quartz, along the direction of 54.5° apart from [1 0 0], a period of 16.91 Å (l_b) exists. It can also be found that $2l_b \approx 5d_{101}$ with a mismatch of 7.0%. This length adaption is not perfect but still acceptable. However, the angle mismatch is only 0.9%. Hence, ST cut quartz might be possible to act as the substrate for the epitaxial growth of crystallized $CH_3NH_3PbI_3$ structures relying on the lattice match between the two materials. Also, the surface structure of X, Y, and Z cut quartz was also investigated as shown in Fig. S1† and the periodic lengths are listed in Table S1.† They do not show a good structural match to the $CH_3NH_3PbI_3$ crystal.

We tried to use the slip-coating[24] method to grow $CH_3NH_3PbI_3$ crystals on the ST cut quartz substrate with DMF (*N*,*N*-dimethyl formamide) solution and a glass slide as the slip. As

[a]Key Laboratory for the Physics and Chemistry of Nanodevices, Beijing National Laboratory of Molecular Sciences, State Key Laboratory of Rare Earth Materials Chemistry and Applications, College of Chemistry and Molecular Engineering, Peking University, Beijing 100871, China. E-mail: yanli@pku.edu.cn

[b]Academy for Advanced Interdisciplinary Studies, Peking University, Beijing 100871, China

[c]Department of Materials Science and Engineering, Peking University, Beijing 100871, China

[d]Electron Microscopy Laboratory, Peking University, Beijing 100871, China

[e]Bruker (Beijing) Scientific Technology Co., Ltd., Beijing 100081, China

† Electronic supplementary information (ESI) available. See DOI: 10.1039/c5ta04936a

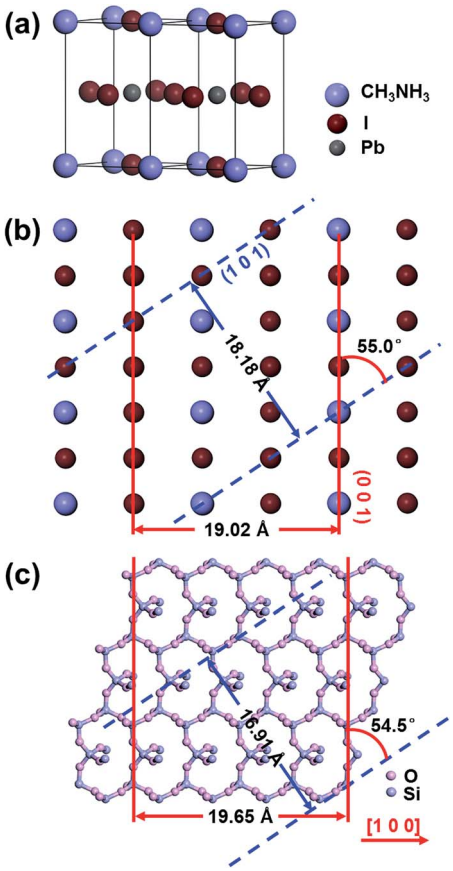

Scheme 1 The structure matching between $CH_3NH_3PbI_3$ and ST cut quartz. (a) Two unit cells of $CH_3NH_3PbI_3$; (b) d_{001} and d_{101} shown on the (0 1 0) plane of $CH_3NH_3PbI_3$; (c) periodical structure on the surface of ST cut quartz.

shown in Fig. 1a and b, aligned microribbon arrays with the length of hundreds of microns were grown on the surface of ST cut quartz. All peaks in the X-ray diffraction (XRD) pattern of the sample can be readily assigned to tetragonal $CH_3NH_3PbI_3$ and the quartz substrate as shown in Fig. S2.† The intensive peaks appearing at 2θ of 13.9°, 14.3°, 28.0°, and 28.6° correspond to diffractions of (0 0 2), (1 1 0), (0 0 4), and (2 2 0) planes of $CH_3NH_3PbI_3$, respectively.[1] This indicates that well crystallized perovskite with good phase purity was formed on quartz. The high resolution transmission electron microscopy (HRTEM) image in Fig. 1d shows fringes perpendicular to the longitudinal direction of the microribbon with the inter-distance of 3.2 Å, which is in good accordance with d_{004} (3.17 Å) of $CH_3NH_3PbI_3$. The Fourier transform pattern of the HRTEM image can also be well ascribed to tetragonal $CH_3NH_3PbI_3$. Therefore the microribbons extend along the [0 0 1] direction or *c* axis of the $CH_3NH_3PbI_3$ crystal.

We also performed slip-coating under the same conditions on X, Y, and Z cut quartz, respectively. On these quartz substrates, $CH_3NH_3PbI_3$ crystals were randomly oriented (Fig. 2b–d). But on ST cut quartz, no matter what direction we moved the slipping slide, the $CH_3NH_3PbI_3$ microribbons were always oriented along the same direction, *i.e.* 45° to the margins of the quartz substrates as shown in Fig. 3. This is the same direction as the aligned SWNT arrays on ST cut quartz and we know it is the [1 0 0] direction of quartz.[32,35] All these facts reveal that the surface lattice of ST cut quartz is responsible for the formation of aligned $CH_3NH_3PbI_3$ ribbons. Taking the HRTEM characterization in Fig. 1 into account, it is obvious that the [0 0 1] direction of $CH_3NH_3PbI_3$ parallels the [1 0 0] direction of quartz. This is in good accordance to what we already predicted in Scheme 1.

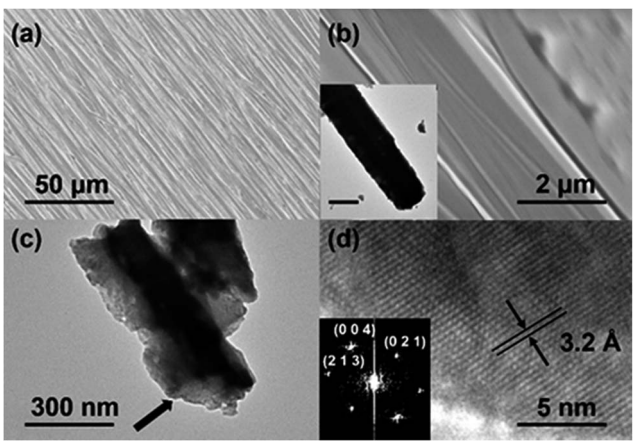

Fig. 1 SEM and TEM characterization of $CH_3NH_3PbI_3$ microribbons formed on ST cut quartz. (a and b) Low (a) and high magnification (b) SEM images. The inset shows the TEM image of a single perovskite microribbon. The bar represents 2 μm. (c and d) TEM (c) and the HRTEM (d) image of the site pointed by the arrow in (c). The corresponding FFT pattern is inserted in (d).

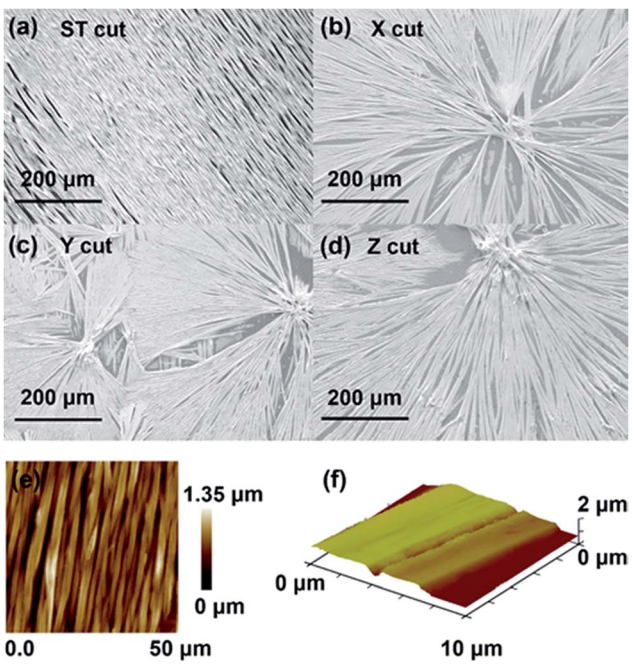

Fig. 2 SEM images of $CH_3NH_3PbI_3$ performed on ST (a), X (b), Y (c), and Z (d) cut quartz and the tapping-mode AFM topographic image (e) as well as the 3D height image (f) of the aligned $CH_3NH_3PbI_3$ arrays at different magnifications.

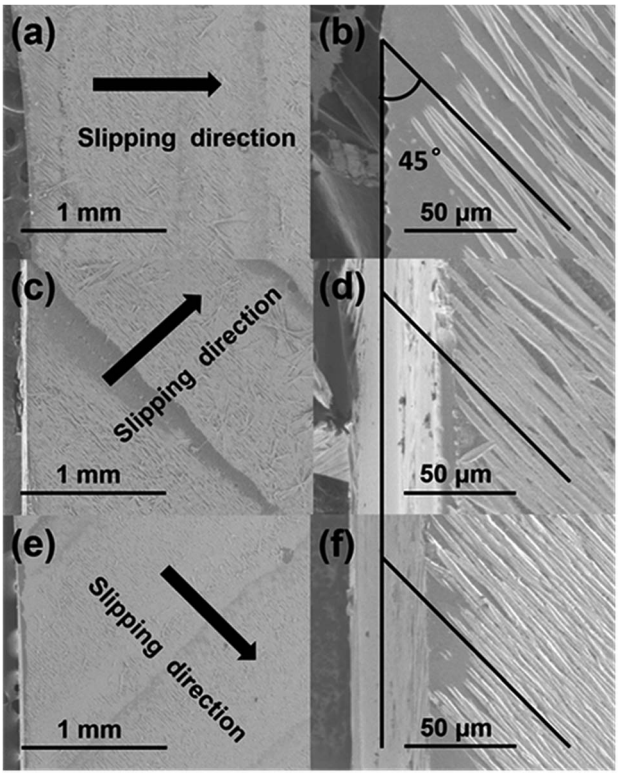

Fig. 3 SEM images of $CH_3NH_3PbI_3$ microribbons fabricated in different slip-coating directions.

We carried out two-dimensional wide angle X-ray diffraction (WAXD) measurements in the 2θ range of 0 to 30° to further verify the structural correlation between $CH_3NH_3PbI_3$ microribbons and the ST cut quartz. In the two-dimensional WAXD images, 2θ is represented by the distance to the center. Blank ST cut quartz only shows one diffraction spot at a 2θ of ~26.6° (Fig. S3†), which was assigned to (1 0 1) planes of ST cut quartz (JCPDS no. 46-1045). This spot also appears in the diffraction patterns of ST cut quartz substrates with $CH_3NH_3PbI_3$ microribbons (Fig. 4c and d). $CH_3NH_3PbI_3$ microribbon arrays presents a strong diffraction spot at ~13.9° (Fig. 4c); while disordered $CH_3NH_3PbI_3$ microribbons only show a weak ring at the same diffraction angle (Fig. 4d), which corresponds to (0 0 2) planes of $CH_3NH_3PbI_3$. This result indicates the good alignment of $CH_3NH_3PbI_3$ microribbon arrays obtained by the slip-coating method. In WAXD patterns, the angle between the (0 0 2) plane of $CH_3NH_3PbI_3$ and the (1 0 1) plane of ST cut quartz is about 43.0°. We know that the angle between (1 0 1) planes and (1 0 0) planes of ST cut quartz is ~42.3°. Therefore, the *c* axis of $CH_3NH_3PbI_3$ microribbons is parallel to the [1 0 0] direction of quartz. The WAXD measurements reveal the orientation of the $CH_3NH_3PbI_3$ crystal on ST cut quartz and provides further evidence for the epitaxial growth mechanism.

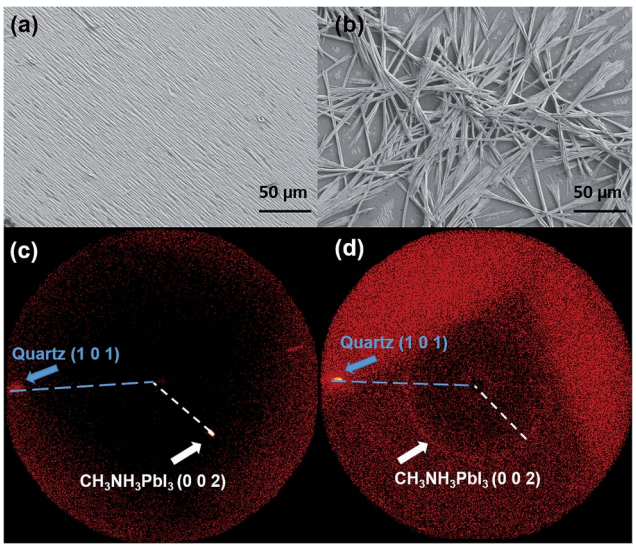

Fig. 4 SEM images, 2D WAXD pattern and XRD patterns of the substrate with aligned $MAPbI_3$ microribbon arrays (a and c) and $CH_3NH_3PbI_3$ microribbons with disordered orientations (b and d).

The thickness of the liquid films on the quartz substrate can be varied by changing the pressure exerted onto the slipping slide, and subsequently the thickness of the $CH_3NH_3PbI_3$ microribbons can be easily adjusted. As shown in Fig. S4,† the average heights have been modulated from ~400 nm to ~2 μm, though some sophisticated techniques are needed to realize a precise control. Fig. 2e and f show the typical AFM images of the $CH_3NH_3PbI_3$ microribbon arrays with a thickness of ~700 nm. The widths of the ribbons are around hundreds of nanometers to several microns.

Because the $CH_3NH_3PbI_3$ microribbons were formed on quartz, the samples are ready for direct detection of the UV-Vis-NIR absorption. The microribbons show intensive and broad absorption from UV to the near IR region until ~800 nm as shown in Fig. S6.† The bandgap was estimated to be ~1.6 eV, which is very similar to the reported values.[1,4]

Au electrodes with a thickness of 60 nm and 8 nm of Cr buffer layer were evaporated directly onto the quartz substrates with $CH_3NH_3PbI_3$ microribbons to fabricate devices and their photo-response performances were studied (Fig. 5). The

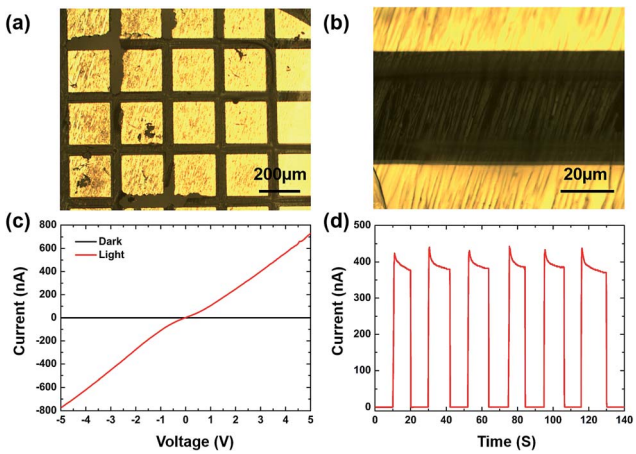

Fig. 5 The devices of $CH_3NH_3PbI_3$ microribbon arrays with Au as electrodes and the photoresponse performance. (a and b) Images of the devices with the electrodes at low and high amplifications; (c and d) *I*–*V* (c) and *I*–*T* (d) characteristics of devices.

channel lengths between two electrodes are about 40 μm and the side lengths of the square Au electrodes are ~200 μm. We measured the *I–T* curves at an ON/OFF interval of ~10 s. The response time of the photocurrent was observed to be ~0.1 s, which actually already reaches the limitation of our detector. The photocurrent of devices built on aligned microribbons is normally 5 times higher than the device of disordered $CH_3NH_3PbI_3$ microribbons (Fig. S5†). In addition, a sample annealed at 80 °C for 2 hours was measured for comparison. No obvious difference in photoresponse performance was observed. This may indicate that $MAPbI_3$ microribbons formed by epitaxial growth are already with considerable crystallinity.

Conclusions

In summary, aligned $CH_3NH_3PbI_3$ array films with high-quality crystallization have been fabricated on ST cut quartz *via* a slip-coating method. The surface lattice of ST cut quartz acts as the template to guide the epitaxial growth of $CH_3NH_3PbI_3$ microribbon arrays. The matching between the lattice spacing of (0 0 1) planes of $CH_3NH_3PbI_3$ and the intervals along the [1 0 0] direction of ST cut quartz leads to the oriented growth of $CH_3NH_3PbI_3$ microcrystals along the [1 0 0] direction of ST cut quartz, resulting in $CH_3NH_3PbI_3$ microribbons extended along the *c* axis. These ribbons are in the length of the sub-millimeter scale, width of microns, and thickness of hundreds of nanometers to several microns depending on the preparation conditions. The elimination of grain boundaries is always desired for perovskite-based devices. The epitaxial growth on ST cut quartz provides a strategy to produce large scale aligned microribbon perovskite films with high crystallinity, which may bring about improved performance. In addition, the alignment of the microribbons should lead to heterogeneous performance along different directions, which can also be made use of in certain applications.

Acknowledgements

We thank Prof. X. Jing for discussion on the crystal structure and Prof. S. Wang for the help in device measurements. This work is supported by the Ministry of Science and Technology of China (Project 2011CB933003) and the National Natural Science Foundation of China (projects 21125103, 91333105, and 21321001).

Notes and references

1 J. H. Im, C. R. Lee, J. W. Lee, S. W. Park and N. G. Park, *Nanoscale*, 2011, **3**, 4088.
2 M. M. Lee, J. Teuscher, T. Miyasaka, T. N. Murakami and H. J. Snaith, *Science*, 2012, **338**, 643–647.
3 Y. X. Zhao and K. Zhu, *J. Am. Chem. Soc.*, 2014, **136**, 12241–12244.
4 L. Etgar, P. Gao, Z. S. Xue, Q. Peng, A. K. Chandiran, B. Liu, M. K. Nazeeruddin and M. Grätzel, *J. Am. Chem. Soc.*, 2012, **134**, 17396–17399.
5 G. Giorgi, J. I. Fujisawa, H. Segawa and K. Yamashita, *J. Phys. Chem. Lett.*, 2013, **4**, 4213–4216.
6 H. J. Snaith, *J. Phys. Chem. Lett.*, 2013, **4**, 3623–4363.
7 H. S. Kim, S. H. Im and N. G. Park, *J. Phys. Chem. C*, 2014, **118**, 5615–5625.
8 S. D. Stranks, G. E. Eperon, G. Grancini, C. Menelaou, M. J. P. Alcocer, T. Leijtens, L. M. Herz, A. Petrozza and H. J. Snaith, *Science*, 2013, **342**, 341–344.
9 G. C. Xing, N. Mathews, S. Y. Sun, S. S. Lim, Y. M. Lam, M. Grätzel, S. Mhaisalkar and T. C. Sum, *Science*, 2013, **342**, 344–347.
10 A. Kojima, K. Teshima, Y. Shirai and T. Miyasaka, *J. Am. Chem. Soc.*, 2009, **131**, 6050–6051.
11 B. V. Lotsch, *Angew. Chem., Int. Ed.*, 2014, **53**, 635–637.
12 N. G. Park, *J. Phys. Chem. Lett.*, 2013, **4**, 2423–2429.
13 M. J. Carnie, C. Charbonneau, M. L. Davies, J. Troughton, T. M. Watson, K. Wojciechowski, H. Snaith and D. A. Worsley, *Chem. Commun.*, 2013, **49**, 7893.
14 J. Burschka, N. Pellet, S. J. Moon, R. H. Baker, P. Gao, M. K. Nazeeruddin and M. Grätzel, *Nature*, 2013, **499**, 316–319.
15 D. Y. Liu and T. L. Kelly, *Nat. Photonics*, 2013, **8**, 133–138.
16 M. Z. Liu, M. B. Johnston and H. J. Snaith, *Nature*, 2013, **501**, 395–398.
17 Q. Chen, H. P. Zhou, Z. R. Hong, S. Luo, H. S. Duan, H. H. Wang, Y. S. Liu, G. Li and Y. Yang, *J. Am. Chem. Soc.*, 2014, **136**, 622–625.
18 H. S. Kim, J. W. Lee, N. Yantara, P. P. Boix, S. A. Kulkarni, S. Mhaisalkar, M. Grätzel and N. G. Park, *Nano Lett.*, 2013, **13**, 2412–2417.
19 H. P. Zhou, Q. Chen, G. Li, S. Luo, T. B. Song, H. S. Duan, Z. R. Hong, J. B. You, Y. S. Liu and Y. Yang, *Science*, 2014, **345**, 542–546.
20 W. Y. Nie, H. H. Tsai, R. Asadpour, J. C. Blancon, A. J. Neukirch, G. Gupta, J. J. Crochet, M. Chhowalla, S. Tretiak, M. A. Alam, H. L. Wang and A. D. Mohite, *Science*, 2015, **347**, 522–525.
21 J. H. Im, J. S. Luo, M. Franckevičius, N. Pellet, P. Gao, T. Moehl, S. M. Zakeeruddin, M. K. Nazeeruddin, M. Grätzel and N. G. Park, *Nano Lett.*, 2015, **15**, 2120–2126.
22 W. S. Yang, J. H. Noh, N. J. Jeon, Y. C. Kim, S. C. Ryu, J. W. Seo and S. I. Seok, *Science*, 2015, **348**, 1234–1237.
23 D. Shi, V. Adinolfi, R. Comin, M. J. Yuan, E. Alarousu, A. Buin, Y. Chen, S. Hoogland, A. Rothenberger, K. Katsiev, Y. Losovyj, X. Zhang, P. A. Dowben, O. F. Mohammed, E. H. Sargent and O. M. Bakr, *Science*, 2015, **347**, 519–522.
24 E. Horváth, M. Spina, Z. Szekrényes, K. Kamarás, R. Gaal, D. Gachet and L. Forró, *Nano Lett.*, 2014, **14**, 6761–6766.
25 M. Law, L. E. Greene, J. C. Johnson, R. Saykally and P. D. Yang, *Nat. Mater.*, 2005, **4**, 455–459.
26 X. J. Feng, K. Shankar, O. K. Varghese, M. Paulose, T. J. Latempa and C. A. Grimes, *Nano Lett.*, 2008, **8**, 3781–3786.
27 M. N. Baibich, J. M. Broto, A. Fert, F. Nguyen Van Dau and F. Petroff, *Phys. Rev. Lett.*, 1988, **61**, 2472–2475.
28 G. Binasch, P. Grünberg, F. Saurenbach and W. Zinn, *Phys. Rev. B: Condens. Matter Mater. Phys.*, 1989, **39**, 4828–4830.

29 C. Berger, Z. M. Song, X. B. Li, X. S. Wu, N. Brown, C. Naud, D. Mayou, T. B. Li, J. Hass, A. N. Marchenkov, E. H. Conrad, P. N. First and W. A. de Heer, *Science*, 2006, **312**, 1191–1196.
30 K. V. Emtsev, A. Bostwick, K. Horn, J. Jobst, G. L. Kellogg, L. Ley, J. L. McChesney, T. Ohta, S. A. Reshanov, J. Röhrl, E. Rotenberg, A. K. Schmid, D. Waldmann, H. B. Weber and T. Seyller, *Nat. Mater.*, 2009, **8**, 203–207.
31 H. B. Chu, L. Ding, J. Y. Wang, X. M. Li, L. P. You and Y. Li, *J. Phys. Chem. C*, 2008, **112**, 18938–18942.
32 L. Ding, D. N. Yuan and J. Liu, *J. Am. Chem. Soc.*, 2008, **130**, 5428–5429.
33 J. Liu, C. Wang, X. M. Tu, B. L. Liu, L. Chen, M. Zheng and C. W. Zhou, *Nat. Commun.*, 2012, **3**, 1199.
34 S. J. Kang, C. Kocabas, T. Ozel, M. Shim, N. Pimparkar, M. A. Alam, S. V. Rotkin and J. A. Rogers, *Nat. Nanotechnol.*, 2007, **2**, 230–236.
35 J. L. Xiao, S. Dunham, P. Liu, Y. W. Zhang, C. Kocabas, L. Moh, Y. G. Huang, K. C. Hwang, C. Lu, W. Huang and J. A. Rogers, *Nano Lett.*, 2009, **9**, 4311–4319.